Journal of Advanced Ceramics
2018, **7**(3): 207–217
https://doi.org/10.1007/s40145-018-0272-6
ISSN 2226-4108
CN 10-1154/TQ

Research Article

Co^{2+} substituted Mg–Cu–Zn ferrite: Evaluation of structural, magnetic, and electromagnetic properties

L. M. THORAT[a], J. Y. PATIL[b], D. Y. NADARGI[b], U. R. GHODAKE[c], R. C. KAMBALE[d], S. S. SURYAVANSHI[b,*]

[a]*Department of Electronics, S. M. Dnyandeo Mohekar Mahavidyalaya, Kalamb - 413507, Maharashtra, India*
[b]*School of Physical Sciences, Solapur University, Kegaon, Solapur - 413255, Maharashtra, India*
[c]*Department of Electronics, Shri Shivaji Mahavidyalaya, Barshi - 413401, Solapur, Maharashtra, India*
[d]*Department of Physics, Savitribai Phule Pune University, Ganeshkhind, Pune - 411007, Maharashtra, India*

Received: January 06, 2018; Revised: March 27, 2018; Accepted: March 28, 2018

Abstract: We report the synthesis of Co^{2+} substituted Mg–Cu–Zn ferrite via citrate gel combustion process and thereby its structural, transport, and magnetic properties for the use in electromagnetic energy absorption application. The polycrystalline ferrite system is investigated by interplay of stoichiometric composition with $Mg_{0.25-x}Co_xCu_{0.25}Zn_{0.5}Fe_2O_4$ ($0 \leqslant x \leqslant 0.25$). Structural investigations using X-ray diffraction (XRD) and selected area electron diffraction (SAED) reveal the formation of spinel structure with linear growth of lattice constant due to Co^{2+} substitution. The microstructural analysis (TEM and SEM) depicts the dense microstructure with the average grain size of 0.42–1.25 μm. The elemental analysis (EDS) confirms the elemental composition of the as-prepared ferrite with respect to the initial concentrations of the synthetic composition used. The observed variations in initial permeability (μ_i) and magnetic moment (n_B) are explained based on deviation in saturation magnetization (M_s), anisotropy constant (K_1), density values, and exchange interaction. The temperature dependence of DC resistivity confirms the semiconducting behavior of the as-prepared ferrite material, with an increase in the DC resistivity by an incorporation of cobalt. Furthermore, the effects of adding Co^{2+} on the Curie temperature, frequency dependent dielectric properties of the ferrite material are also discussed.

Keywords: Co–Mg–Cu–Zn ferrite; spinel phase; electrical resistivity; saturation magnetization; anisotropy constant; Curie temperature

1 Introduction

Modern technology can be considered as a direct consequence of the innovations made and research carried out in the fields of science and engineering. The uncontrolled and progressive growth of modern communication technologies associated with increased industrialization is exploded into one of the biggest crisis of pollution, i.e., electromagnetic pollution or electrosmog. The chronology of exponential growth of microwave usage starts from military applications (RADAR) in 1939 to RF-based systems in 2016. The most frequent culprits are right at the home: TV,

* Corresponding author.
E-mail: sssuryavanshi@rediffmail.com

wireless phones, home appliances, Wi-Fi systems, AC systems, and many more. Therefore, there is an imperative call for the development of electromagnetic wave absorbers with wider absorbing bandwidth [1–7]. By an impedance match of absorber, electromagnetic effect can be nullified through heat dissipation by magnetic and dielectric losses [8].

Spinel ferrites stand as promising candidates for absorbing electromagnetic energy in VHF/UHF region due to their characteristic features of large magnetic losses (in the range of 155–920 kW/m^3) and large resistivity (3×10^6 Ω·m) [9–11]. Among the various spinel ferrites, Ni–Cu–Zn ferrites were intensively studied due to their high resistivity, low dielectric loss, high Curie temperature, and excellent microwave-absorbing properties [12]. However, Ni–Cu–Zn ferrites are still facing certain inherent problems like sensitivity to stress, high magnetostriction constant, and carcinogenic nature of nickel [13,14]. As an alternative to Ni–Cu–Zn ferrites, Mg–Cu–Zn ferrites have attracted researchers' attention due to their fascinating properties, such as high resistivity, relatively high Curie temperature, high mechanical hardness, low production cost, environmental stability, and pertinent magnetic material [15,16]. Cobalt ferrite nanopowders are the subject of much interest due to their electrical and magnetic properties compared to their bulk counterparts [2]. Co^{2+} is a fast-relaxing ion which can enhance microwave properties. It is the anisotropic ion responsible for the magnetic response time. These properties along with their physical and chemical stability make them suitable for applications in magnetic recording, as magnetic fluids, and for magnetic drug delivery.

Several synthetic routes were employed for the development of aforementioned mixed ferrite system, namely sol–gel [17], hydrothermal [18], mechanochemical [19], and auto-emulsion [20] methods. Here, we adopt simple and straightforward strategy of developing Co^{2+} substituted Mg–Cu–Zn ferrite using citrate gel auto-combustion route. The route is more promising over the other preparative techniques, due to fine control over the stoichiometry, homogeneity, elemental composition, and morphology of the final compound. In the present work, the investigation is aimed to develop the ferrite material ($Mg_{0.25-x}Co_xCu_{0.25}Zn_{0.5}Fe_2O_4$ ($0 \leqslant x \leqslant 0.25$)) and characterize its structural, morphological, electrical, and magnetic properties for electromagnetic wave absorbing application.

2 Experimental details

As mentioned, the citrate gel combustion method was utilized to synthesize $Mg_{0.25-x}Co_xCu_{0.25}Zn_{0.5}Fe_2O_4$ ($0 \leqslant x \leqslant 0.25$) ferrite powders. The general approach of synthesizing Co^{2+} substituted Mg–Cu–Zn ferrites involves two major steps: (i) synthesis of material powders by citrate gel combustion process and formation of pellets and/or toroids, and (ii) characterization of as-prepared material.

2.1 Synthesis

In a typical synthesis, AR grade nitrates (magnesium nitrate ($Mg(NO_3)_2\cdot6H_2O$), cobalt nitrate ($Co(NO_3)_2\cdot6H_2O$), copper nitrate ($Cu(NO_3)_2\cdot6H_2O$), zinc nitrate ($Zn(NO_3)_2\cdot4H_2O$), ferric nitrate ($Fe(NO_3)_3\cdot9H_2O$), and citric acid ($C_6H_8O_7$) were used as raw materials. The synthetic molar ratio of metal nitrates to fuel was kept constant at 3:5, and the doping of Co was varied in the range of $0 \leqslant x \leqslant 0.25$, where the system is $Mg_{0.25-x}Co_xCu_{0.25}Zn_{0.5}Fe_2O_4$. Citric acid served the role of fuel.

The intentions of using fuel-rich composition (3:5) are: (i) the fuel (citric acid) serves as a complexing agent, which limits the precipitation of individual precursor moieties prior to ignition. Due to its higher concentration in the synthetic mixture and specific chemical nature, the homogeneity in the reaction is enhanced widely, which is important in the present complex-material fabrication; (ii) to prevent from agglomeration; and (iii) importantly, in order to have a controlled and complete heat of combustion [21].

The introduction of Cu^{2+} in the present ferrite system leads to considerable densification (94%) of theoretical density. This increase in density may be attributed to: (i) the acceleration of cation interdiffusion due to Cu^{2+} ions, and (ii) the increase in the reactivity of fine ferrite grains which coalesce to form bigger grains, reduced pores, and volume shrinkage. Therefore, in the present system, the Cu content was kept constant at 25 at%.

Once the chemical constituents were well mixed in appropriate amount of distilled water, the precursor solution was heat treated at 100 ℃, till it got converted into gel. The resultant gel was continued to heat treat at higher temperature (150–200 ℃). The viscous gel began frothing and eventually after water evaporation, the gel started exhausting into fast flameless auto-combustion reaction with the evolution of large number of gaseous products after which it got

ignited. The obtained powders were calcinated at 500 ℃ for 2 h to remove the traces of unreacted leftovers, and retain the pure ferrite material. The powders were then made into pellets (15 mm in diameter and 2 mm in thickness) and toroids (inner diameter = 1.5 cm, outer diameter = 2.5 cm, average height = 0.3 cm) with hydraulic pressing machine (pressure = 1.5 ton/cm^2, binder: PVA). In the end, both pellets and toroids were sintered at 700 ℃ for 2 h in air.

2. 2 Characterization

Crystallographic identification of as-prepared ferrites was done using XRD analysis (Bruker D8 advance, Karlsruhe, Germany). The XRD signatures were obtained using Cu Kα (λ = 1.5405 Å) radiation at 2θ values between 20° and 80°. The interplanar distance d was calculated using Bragg's law. The lattice constant a of ferrite samples was calculated using the formula for interplanar spacing $\frac{1}{d^2}=\frac{h^2+k^2+l^2}{a^2}$ [22], where d is the interplanar spacing, h, k, and l are the Miller indices of the crystal plane. The average crystallite size was calculated by using Scherrer's formula [23], $t=0.9\lambda/\beta\cos\theta$, where t is the crystallite size, β is the full width at half maximum (FWHM) of most intense (311) peak, θ is the angle of diffraction, and λ is the X-ray wavelength (1.5405 Å).

The X-ray density, bulk density, and relative density were calculated by $\rho_{\mathrm{x}}=\frac{ZM}{Na^3}$, where Z is the number of molecules per unit cell, M is the molecular weight, N is the Avogadro's number (6.023×10^{23} mol^{-1}), a is the lattice constant, and $\rho_{\mathrm{m}}=\frac{m}{\pi r^2 h}$, where m is the mass, r is the radius, and h is the thickness of the pellet. The morphological analysis was done by using electron microscope (SEM, Model 6306A JEOL-JSM, Japan; TEM, Philips CM 200 FEG). Percentage of porosity P of the ferrite samples was calculated from ρ_{m} and ρ_{x} values using the expression $P=\left(1-\frac{\rho_{\mathrm{m}}}{\rho_{\mathrm{x}}}\right)\times100\%$.

DC resistivity measurements were carried out with two-probe method. The equation used for the determination of resistivity is $\rho_{\mathrm{DC}}=\frac{\pi r^2 R}{t}$. A vibrating sample magnetometer (Lake Shore 7410 VSM) was used to study the magnetization measurements of the ferrite samples, and the magnetic hysteresis loops were obtained with an applied magnetic field of 20 kOe. The double coil set up [24] was used to study the susceptibility measurements on powders of ferrite samples. The inductance measurements were carried out on toroidal shape samples of ferrite from room temperature to 350 ℃ at 1 kHz using an impedance analyzer (Hioki Model 3532-50 LCR HiTester, Japan). Also, the frequency dispersion of initial permeability (μ_{i}) was studied in frequency range of 100 Hz to 5 MHz at room temperature. The initial permeability of the ferrite samples was calculated using the inductance data and the standard formula for initial permeability [23]. The dielectric measurements at room temperature were carried using LCR-Q meter (HP 4284). The temperature variation curves of susceptibility and initial permeability were referred for the determination of the Curie temperature values.

3 Results and discussion

3. 1 Structural analysis

Figure 1 illustrates the Bragg reflection signatures of $Mg_{0.25-x}Co_xCu_{0.25}Zn_{0.5}Fe_2O_4$ ($0 \leqslant x \leqslant 0.25$) ferrites. The spectra show the presence of peaks that correspond to (220), (311), (222), (400), (422), (511), (440), and (531) planes, where highly intense peak at (311) plane confirms cubic spinel structure of as-prepared material [16]. The reflection patterns are in well agreement with the standard JCPDS Card No. 08-0234. The lattice constant (a) is found to increase (little and logical) with increase in Co^{2+} content, due to its larger ionic radius (0.72 Å) as compared to Mg^{2+} (0.71 Å). The crystallite size is calculated only from

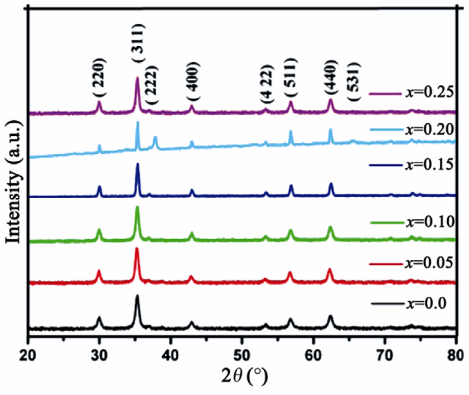

Fig. 1 XRD patterns of the $Mg_{0.25-x}Co_xCu_{0.25}Zn_{0.5}Fe_2O_4$ ($0 \leqslant x \leqslant 0.25$) ferrites.

Table 1 Data on lattice constant (a), crystallite size (t), bulk density (ρ_m), X-ray density (ρ_x), relative density (ρ_r), grain size (D), particle size (t_1) from TEM, Curie temperature from DC resistivity (T_C) of $Mg_{0.25-x}Co_xCu_{0.25}Zn_{0.5}Fe_2O_4$ ferrites

No.	Content of Co x	Lattice constant a (Å)	Crystallite size t (nm)	Grain size D from SEM (μm)	Particle size t_1 from TEM (nm)	T_C from DC resistivity (℃)	Density		
							Bulk ρ_m (g/cm^3)	X-ray ρ_x (g/cm^3)	Relative ρ_r (%)
1	0	8.394	50	0.42	281	144	4.39	5.17	85
2	0.05	8.446	48	1.40	547	153	4.18	5.11	93
3	0.10	8.401	50	2.02	243	182	4.81	5.23	92
4	0.15	8.381	49	1.58	342	192	4.83	5.31	91
5	0.20	8.409	51	1.33	218	194	4.86	5.29	92
6	0.25	8.395	47	1.25	112	227	4.98	5.36	93

(311) peak. The lattice constant (a), crystallite size (t), bulk density, X-ray density, and relative density values of all the compositions are tabulated in Table 1.

The crystallite size varies from 47 to 51 nm. The observed variation in crystallite size of Co^{2+} substituted Mg–Cu–Zn ferrites supports the observed lattice constant variation results. Relative density increases with Co^{2+} substitution, exhibiting maximum (93%) for x = 0.05. As magnesium has lower atomic weight (24.30 amu) than cobalt (58.93 amu), the relative density of the sample without Co doping (x = 0) is observed lower than that of Co doping (x = 0.25) sample. Further, X-ray density of all the ferrite samples is higher than the corresponding bulk density, due to the existence of the voids and pores [25]. The irregularity in the particle size is observed due to adopted synthesis strategy. At the ignition point, large amount of heat is generated and combustion takes place. The heat generated is quite large for few seconds, and completes the reaction. Hence, due to short lived combustion reaction, there is formation of irregular/ agglomerated size magnetic fine particle clusters.

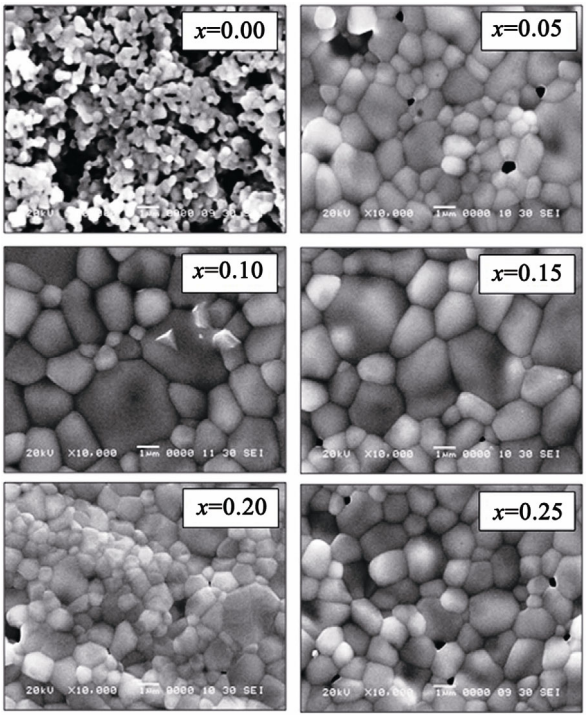

Fig. 2 SEM images of $Mg_{0.25-x}Co_xCu_{0.25}Zn_{0.5}Fe_2O_4$ ($0 \leqslant x \leqslant 0.25$) ferrites.

3. 2 Morphological properties

The microstructure analyses of as-prepared ferrites were done using SEM and TEM. The formation of compact microstructure is observed for the Co^{2+} substituted ferrite samples (Fig. 2). However, the control experiment (x = 0) shows the imperfect network formation (Fig. 2(a)). The average grain size (D) was determined using the line intercept method (Table 1). Enhancement in the grain size is observed with the addition of Co^{2+} to Mg^{2+} ions in $Mg_{0.25-x}Co_xCu_{0.25}Zn_{0.5}Fe_2O_4$ samples. The micrographs of Co^{2+} doped ferrite samples show the formation of distinct grains. The maximum grain size is observed for the ferrite sample with x = 0.10. The non-uniformity in grain size and shape is primarily due to Cu ion liquid phase sintering.

The presence of copper strongly affects the microstructure of the ferrite sample because it facilitates the liquid phase sintering. The grain growth can be considered as competition between the driving force for grain boundary movement and the retarding force exerted by pores [26]. During sintering, the thermal energy generates a force that drives the grain boundaries to grow over pores, thereby decreasing the pore volume and making the material dense. If the driving force on each grain is homogeneous, then the uniform distribution of the grain size takes place. However, if the driving force is nonhomogenous, then abnormal grain growth will occur. The non-uniformity of the grain size in the present study is due to the non-homogeneous driving force on the grains [27]. Moreover, another possibility for the formation of

liquid phase will be the adopted synthesis strategy. During the combustion reaction, the temperature of the reactants reaches ~1000 ℃ for short time (few seconds), which undoubtedly facilitates the liquid phase formation. However, the obtained microstructure of the developed material is useful for attaining good electromagnetic properties like permeability and magnetization.

Figure 3 shows the EDS spectra for $Mg_{0.25-x}Co_xCu_{0.25}Zn_{0.5}Fe_2O_4$ ferrite with x = 0.20, which confirms the presence of its constituents. The corresponding EDS data is tabulated in Table 2.

In addition to SEM analysis, particle size (t_1) and nanostructure of Co^{2+} substituted Mg–Cu–Zn ferrite nanoparticles were examined through TEM (Fig. 4). The images are self-explanatory of particle aggregation. The aggregates are the result of cumulative effect of surface tension by magnetostatic interactions amongst the particles [27]. However, the ferrite sample with x = 0.25 exhibits spherical shape. The maximum particle size (547 nm) is observed for the sample with x = 0.05. The particle size measured from TEM studies is in consistent with XRD analysis. The SAED pattern (Fig. 4) confirms the presence circular bright spots (ring structure) corresponding to various planes as represented in XRD pattern and confirms the polycrystalline nature of the ferrite samples.

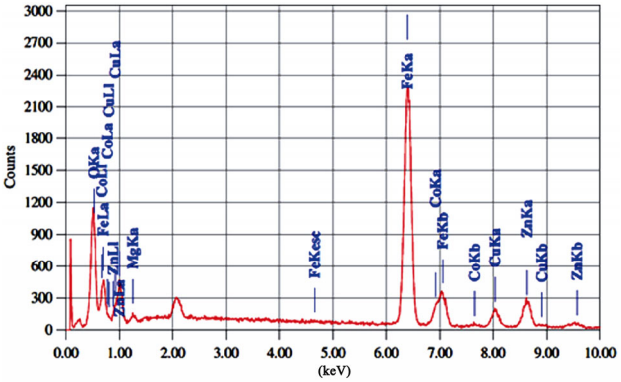

Fig. 3 Typical EDS spectra for $Mg_{0.25-x}Co_xCu_{0.25}Zn_{0.5}Fe_2O_4$ ferrite with x = 0.20.

Table 2 Elemental composition obtained from EDS data for ferrites

No.	Element	Atomic percentage (at%)					
		x = 0	x = 0.05	x = 0.10	x = 0.15	x = 0.20	x = 0.25
1	Mg	4.51	3.58	2.50	1.56	0.88	—
2	Co	—	0.89	1.66	2.67	3.29	4.47
3	Cu	4.33	4.55	4.34	4.73	4.28	4.23
4	Zn	8.73	8.32	8.61	8.92	8.57	8.17
5	Fe	37.08	35.96	33.34	36.96	34.95	35.11
6	O	45.35	46.70	49.55	45.16	48.03	48.02

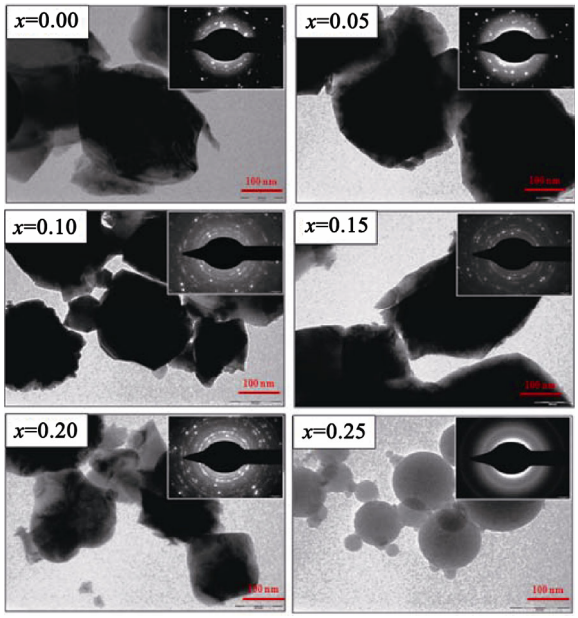

Fig. 4 TEM images of $Mg_{0.25-x}Co_xCu_{0.25}Zn_{0.5}Fe_2O_4$ ($0 \leqslant x \leqslant 0.25$) ferrites.

3.3 Transport property

Figure 5 shows the variation of logarithm of DC resistivity as a function of reciprocal of temperature for various compositions of $Mg_{0.25-x}Co_xCu_{0.25}Zn_{0.5}Fe_2O_4$ ($0 \leqslant x \leqslant 0.25$) ferrites. With an increase in the temperature, the DC resistivity of the ferrites gets decreased. The semiconducting behavior is observed with the variation in resistivity values due to Co^{2+} substitution.

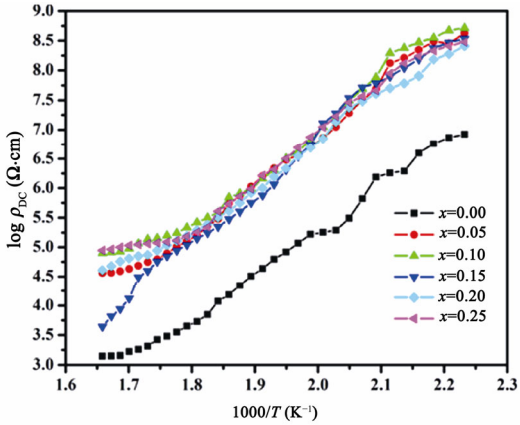

Fig. 5 DC resistivity ($\log \rho_{DC}$) as a function of temperature (1000/T) for all the ferrites.

The room temperature DC resistivity is found to increase with the substitution of cobalt. The maximum DC resistivity is observed in the ferrite sample with x = 0.10. In the compositional substitution for x = 0.10, the change in the cationic distribution would be more, resulting in higher resistivity values. Moreover, the conduction in the ferrites is attributed to the hopping of electrons from Fe^{3+} to Fe^{2+} ions. The number of such ion-pairs depends upon the sintering conditions and the amount of reduction of Fe^{3+} to Fe^{2+} at elevated temperatures. As the resistivity of ferrite is controlled by the Fe^{2+} concentration on the B-site, at x = 0.10, Fe^{2+} concentration might be increased, resulting in higher resistivity.

3. 4 Dielectric properties

The dielectric constant measurements were carried out in the frequency range from 100 Hz to 1 MHz. The variation of dielectric constant (ε') as a function of frequency for $Mg_{0.25-x}Co_xCu_{0.25}Zn_{0.5}Fe_2O_4$ ferrites is shown in Fig. 6(a). For all the ferrite samples, the dielectric constant decreases rapidly with an increase in frequency, and finally remains constant at higher frequencies, showing the ferrimagnetic character. The incorporation of Co^{2+} into Mg–Cu–Zn ferrites has significantly affected the dielectric constant and at higher frequency dielectric constant exhibits composition independent behavior.

The frequency dependent dielectric constant guides the electrons in the direction of the applied field, and thereby polarization. Beyond a certain frequency limit, electron exchange $Fe^{2+} \Leftrightarrow Fe^{3+}$ cannot follow the alternating field. This gives rise to decrease in polarization with increasing frequency up to optimum and attains the steady state. The large value of dielectric constant at lower frequency is due to the predominance of Fe^{2+} ions, interfacial dislocation piles, oxygen vacancies, grain boundary defects, etc. [28], while the decrease in dielectric constant with frequency is because all the above contributing factors to polarizability lag the applied field at higher frequencies.

The complex dielectric constant (ε'') as a function of frequency for $Mg_{0.25-x}Co_xCu_{0.25}Zn_{0.5}Fe_2O_4$ ($0 \leqslant x \leqslant 0.25$) ferrites is shown in Fig. 6(b). For all the samples, complex dielectric constant decreases initially with increase in frequency and reaches a constant value at higher frequency. After further increase in frequency,

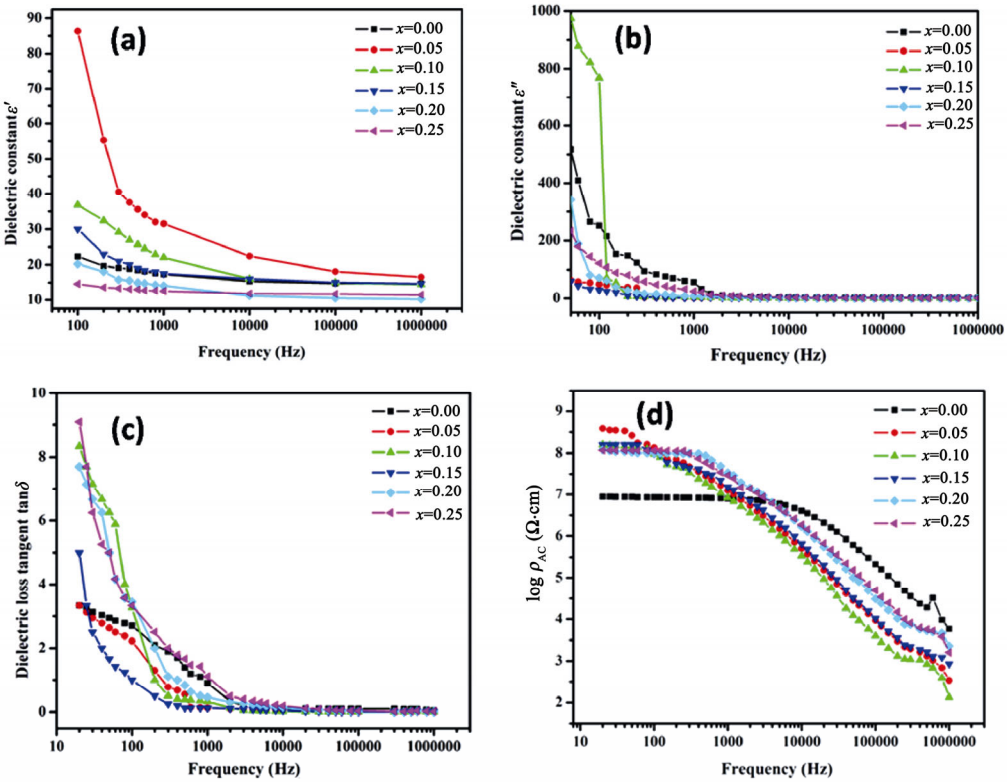

Fig. 6 Dielectric properties of the ferrites as a function of frequency: (a) dielectric constant ε', (b) complex dielectric constant ε'', (c) dielectric loss tangent $\tan\delta$, and (d) AC resistivity ρ_{AC}.

samples respond independently to frequency variation. This behavior is due to the existence of Maxwell–Wagner interfacial polarization, which exists in the inhomogeneous dielectrics [29].

Figure 6(c) shows the dielectric loss tangent ($\tan\delta$) as a function of frequency (100 Hz–1 MHz) for all the prepared ferrites. The dielectric loss tangent decays with increasing frequency up to a certain optimum and remains constant at higher frequencies. The initial decrease in $\tan\delta$ values can be explained based on phenomenological model. The dielectric losses in ferrites are generally reflected in the resistivity, i.e., materials with low resistivity exhibit high dielectric loss and vice versa [23]. The decrease of loss tangent with increasing Co content is due to the exchange of electrons between Fe^{2+} and Fe^{3+}, which is responsible for the conduction mechanism in ferrites.

The response of AC resistivity to external applied field frequency for all ferrite samples is shown in Fig. 6(d). Decrease in AC resistivity with increase in frequency is observed for all the ferrite samples. At lower frequency, the grain boundaries are more active, and hence the hopping frequency of electrons between Fe^{3+} and Fe^{2+} ions is less. At higher frequencies, the conductive grains become more active by promoting the hopping of electrons between Fe^{3+} and Fe^{2+} ions therefore increasing the hopping frequency [30].

3. 5 Magnetic properties

3.5.1 AC susceptibility studies

The normalized AC susceptibility (χ_T / χ_{RT}) of $Mg_{0.25-x}Co_xCu_{0.25}Zn_{0.5}Fe_2O_4$ ($0 \leqslant x \leqslant 0.25$) ferrite samples as a function of temperature is depicted in Fig. 7(a). The normalized susceptibility of as-prepared ferrites almost remains constant up to certain temperature and thereafter a sharp decrease in the susceptibility values is observed up to near Curie temperature. This indicates the absence of impurity phases in the ferrite samples which is also confirmed from XRD studies. The undisturbed normalized susceptibility up to Curie temperature is because the available thermal energy is not sufficient to disturb the aligned moments of spins. This behavior has confirmed the ferrimagnetic nature of as-prepared ferrites. However, above the Curie temperature, the decrease in susceptibility is attributed to the disturbance in moment alignment. This is an indication of ferrimagnetic to paramagnetic state transition. Further, the temperature invariance of normalized AC susceptibility up to Curie temperature for ferrite samples confirms the multi-domain particles' composition.

The values of Curie temperature for all the ferrite samples are given in Table 3. The Curie temperature is found to increase with increase in cobalt content in Mg–Cu–Zn ferrite due to the replacement of nonmagnetic Mg^{2+} ions by Co^{2+} ions which causes the increase in ferrimagentic region, and at the same time the decrease in paramagnetic region. It is because the Co^{2+} has preference occupancy at octahedral site and when it replaces the Mg^{2+} at octahedral site, an enhancement in magnetic interaction at octahedral site occurs [31]. Above the Curie temperature, a complete disordered state as well as the magnetization destruction is observed. The strong exchange interaction in the case of ferrite sample with x = 0.25 due to high content of Co^{2+} results in the highest Curie temperature compared to the other samples.

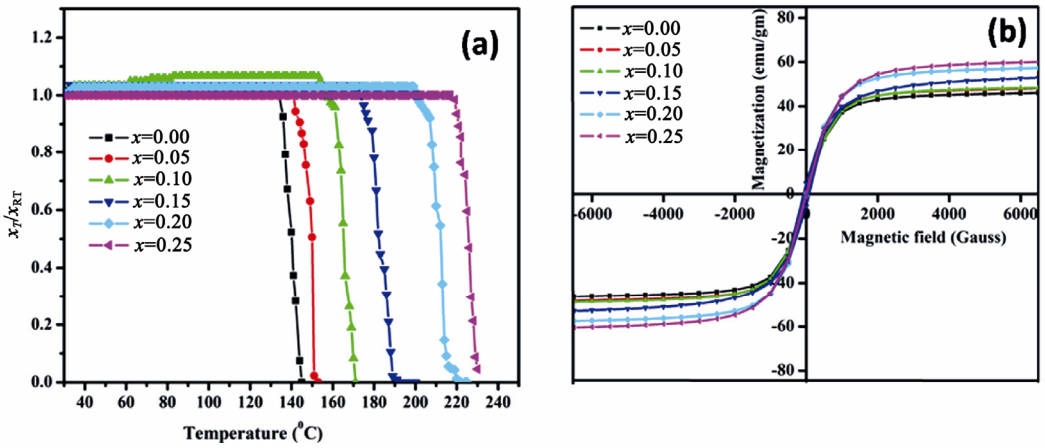

Fig. 7 Magnetic properties of the ferrites: (a) normalized AC susceptibility (χ_T / χ_{RT}) as a function of temperature, and (b) magnetic hysteresis loops.

Table 3 Data on magnetic parameters like saturation magnetization (M_s), M_r/M_s, coercivity (H_c), initial permeability (μ_i), rotational permeability (μ_{rk}), wall permeability (μ_w), magneto crystalline anisotropy constant (K_1), thermal hysteresis of initial permeability, Curie temperature (T_C) from χ_{AC} and μ_i for all the ferrites

No.	Content of Co x	M_s (emu)	M_r/M_s	H_c (G)	μ_i	μ_{rk}	μ_w	μ_{ih}	μ_{ic}	$\Delta\mu_i$	K_1 (10^{-4}erg/mL)	T_C from χ_{AC} (℃)	T_C from μ_i (℃)
1	0.00	239	0.0038	3.41	1268	12	1257	1360	1402	42	–2.50	142	140
2	0.05	251	0.0056	5.16	2466	30	2437	3122	3185	63	12.63	153	150
3	0.10	259	0.0082	7.88	947	13	935	1500	1579	79	27.83	170	190
4	0.15	311	0.0116	11.04	748	11	738	1304	1389	85	43.03	190	200
5	0.20	288	0.0160	18.44	574	13	562	898	987	89	58.23	221	220
6	0.25	329	0.0200	21.36	365	11	355	1000	1093	93	73.43	230	231

3.5.2 Magnetization

The preferential occupancy of the cations, composition, microstructure, and density of ferrites strongly influence their magnetic properties like saturation magnetization, coercivity, and remenance. The typical hysteresis loops of as-prepared ferrites at room temperature are shown in Fig. 7(b). The magnetic hysteresis confirms the prepared ferrite material is magnetically ordered. The values of saturation magnetization (M_s), coercivity (H_c), and remenance for all the ferrite compositions are given in Table 3.

An increase in Co^{2+} content results in increase in the saturation magnetization. Maximum value of saturation magnetization is shown by $Mg_{0.25-x}Co_xCu_{0.25}Zn_{0.5}Fe_2O_4$ ferrite with $x = 0.25$. The magnetic moment of Mg^{2+} is zero whereas the magnetic moment of Co^{2+} is 3.7 μ_B. As the magnetic moment of Co^{2+} is larger than that of Mg^{2+}, there is increase in saturation magnetization. Mg^{2+} and Co^{2+} have inversion degree of 0.8 and 1, respectively, and both prefer the octahedral site. The substitution of Co^{2+} to octahedral site increases the magnetic moment of octahedral site. The magnetic moment per formula unit, according to Neel's two-sublattice model is given by the difference of magnetic moment of each sublattice and can be expressed as [32]: $M = M_A - M_B$, where M_A and M_B are the A- and B-sublattice magnetic moments in μ_B, respectively.

The magnetic moment in ferrites is mainly from the parallel uncompensated electron spin of the individual ions, and the spin alignments in the two sublattices are arranged antiparallel. Also, the A–B exchange interaction is predominant over the A–A and B–B interactions [33]. The saturation magnetization of Co–Cu–Zn ($x = 0.25$) is larger than Mg–Cu–Zn ($x = 0$) which is attributed to the high magnetic moment and high magneto-crystalline anisotropy exhibited by Co [34]. However the relative density of Mg–Cu–Zn ferrite is larger as compared to Co–Cu–Zn ferrite which confirms the high sintering ability of Mg–Cu–Zn ferrite.

The enhancement in saturation magnetization is mainly due to the substitution of magnetic Co^{2+} ions with nonmagnetic Mg^{2+} ions. The observed variation in saturation magnetization can be explained based on cation distribution and the exchange interactions between A- and B-sites. In Mg–Cu–Zn ferrite, the stable Zn^{2+} ions occupy the A-sites only. By substituting Co^{2+} ions for Mg^{2+} on the octahedral sites (B-sites), an increase in the magnetization of B sub-lattice takes place, which leads to increased saturation magnetization of the material.

This is due to the fact that, Co^{2+} strongly influences the coercivity. Moreover, the crystallite size and particle size also influence the coercivity. If the volume of the particle is reduced in such a way that it contains only single domain, then its change in magnetization takes place by rotation only, as a result of which the coercivity increases. The coercivity (H_c) in general is a measure of magnetization reversal process under the action of an applied field and depends strongly on particle size and crystalline anisotropy constant.

The values of experimental magnetic moment (n_B) (expt.), theoretical n_B (th.), and probable cation distribution are given in Table 4. The experimental magnetic moment is increased with increase in Co^{2+} content; however, α_{y-k} is decreased. The decrement in α_{y-k} is attributed to the replacement of nonmagnetic Mg^{2+} ions by magnetic Co^{2+} ions which leads to enhancement in exchange interaction.

Table 4 Probable cation distribution and the magnetic moments of all the ferrites

No.	Content of Co x	Cation distribution	n_B (th.) (μ_B)	n_B (expt.) (μ_B)	$\alpha_{y\text{-}k}$
1	0.00	$(Mg_{0.025}Cu_{0.025}Zn_{0.5}Fe_{0.45})^A$ $[Mg_{0.225}Cu_{0.225}Fe_{1.55}]^BO_4$	5.999	1.94	59˚16'12"
2	0.05	$(Mg_{0.020}Cu_{0.020}Zn_{0.5}Fe_{0.46})^A$ $[Co_{0.05}Mg_{0.180}Cu_{0.230}Fe_{1.54}]^BO_4$	6.014	2.03	58˚23'56"
3	0.10	$(Mg_{0.015}Cu_{0.015}Zn_{0.5}Fe_{0.47})^A$ $[Co_{0.10}Mg_{0.135}Cu_{0.235}Fe_{1.53}]^BO_4$	6.048	2.07	58˚8'25"
4	0.15	$(Mg_{0.010}Cu_{0.010}Zn_{0.5}Fe_{0.48})^A$ $[Co_{0.15}Mg_{0.090}Cu_{0.240}Fe_{1.52}]^BO_4$	6.082	2.46	54˚56'42"
5	0.20	$(Mg_{0.005}Cu_{0.005}Zn_{0.5}Fe_{0.49})^A$ $[Co_{0.20}Mg_{0.045}Cu_{0.245}Fe_{1.51}]^BO_4$	6.121	2.31	56˚53'48"
6	0.25	$(Cu_{0.0025}Zn_{0.5}Fe_{0.4975})^A$ $[Co_{0.25}Cu_{0.2475}Fe_{1.5025}]^BO_4$	6.168	2.61	53˚53'53"

3.5.3 Initial permeability studies

Figure 8(a) shows the variation of initial permeability (μ_i) as a function of frequency (100 Hz–5 MHz) for the ferrite samples of $Mg_{0.25-x}Co_xCu_{0.25}Zn_{0.5}Fe_2O_4$ ($0 \leqslant x \leqslant 0.25$). The initial permeability values display a steady state for certain value of frequency and then increases exponentially with further increase in the frequency. This behavior of initial permeability seems to be in accordance with the magnetocrystalline anisotropy. Table 3 shows the initial permeability (μ_i) values measured at room temperature for 1 kHz frequency, and the initial permeability values during heating and cooling cycles and $\Delta\mu_i$. The initial permeability is found to be dependent on the amount of Co^{2+} substitution. The μ_i value increases with the Co^{2+} substitution up to x = 0.05, and then decreases with further increase in Co^{2+} substitution. Grain size and anisotropy simultaneously affect the permeability. The behavior is mainly attributed to the increase in magnetostriction constant due to substitution of Mg^{2+} by Co^{2+} ions [35].

The response of initial permeability of as-prepared ferrites is investigated at different temperature values. The initial permeability exhibits a steady behavior up to a particular temperature, achieves a peak value, and then suddenly drops to a minimum value at Curie temperature. The sudden fall in initial permeability at Curie temperature is due to the transition of ferrimagnetic state to paramagnetic state. $Mg_{0.25-x}Co_xCu_{0.25}Zn_{0.5}Fe_2O_4$ ferrite with x = 0.05 exhibits maximum initial permeability, and with further increase in Co^{2+} content decrease in permeability is observed. The Curie transition temperature (T_C) is measured from Fig. 8(b) and their values are presented in Table 3. The magnitude of Curie temperature increaseds with Co^{2+} content in Mg–Cu–Zn ferrite. This increase in Curie transition temperature is due to the substitution of magnetic Co^{2+} ions in place of nonmagnetic Mg^{2+} ions at octahedral site. The rotational (μ_{rk}) and wall (μ_w) permeabilityvalues are calculated using the formula:

$$T\mu_{rk} = 1 + 2\pi M^2 s / |k_1|$$

$$\mu_w = \mu_i - (\mu_{rk} - 1)$$

The rotational permeability and wall permeability values are given in Table 3. The magnitude of wall permeability μ_w is very large in comparison with rotational permeability μ_{rk} for all compositions of $Mg_{0.25-x}Co_xCu_{0.25}Zn_{0.5}Fe_2O_4$ ferrite. Thus, it is observed that the main contribution to the initial permeability is due to domain wall motion. All the ferrite samples have exhibited the thermal hysteresis of initial permeability and $\Delta\mu_i$ increases with substitution of cobalt.

In the ferrite materials, magnetic losses are due to phase lag of domain wall motion with respect to the applied AC magnetic field. The variation of magnetic loss factor with temperature is shown in Fig. 8(c). For all the ferrite samples, the loss factor almost remains constant up to a certain temperature; thereafter a drastic increase in the loss factor is observed. It is well known that the higher the value of initial permeability, the lower the value of loss factor, and accordingly the sample with x = 0.05 exhibits the lowest value of loss factor at room temperature.

4 Conclusions

In conclusion, the fine particles of $Mg_{0.25-x}Co_xCu_{0.25}Zn_{0.5}Fe_2O_4$ ($0 \leqslant x \leqslant 0.25$) ferrites were successfully synthesized using citrate gel auto-combustion route. The properties of parent ferrite were improved by the addition of cobalt. Structural analyses

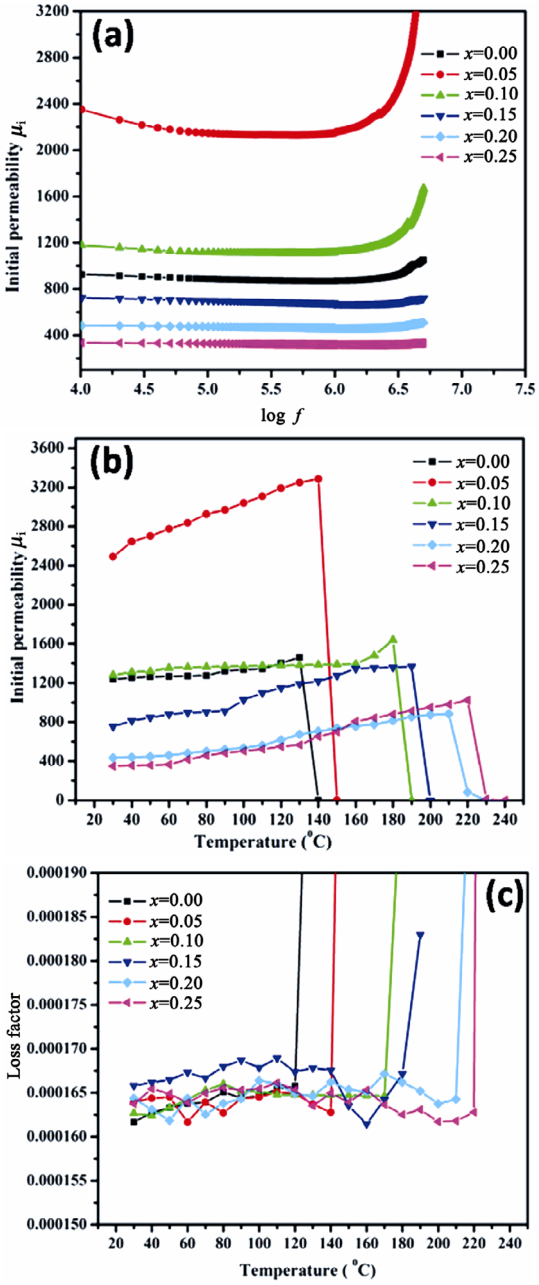

Fig. 8 Permeability studies of the ferrites: (a) frequency dependency of initial permeability μ_i, and (b, c) temperature dependency of permeability and loss factor.

revealed the formation of compact microstructures of all the ferrites. The substitution of Co^{2+} ions showed strong impact on the electric transport, dielectric, and magnetic properties of the parent ferrite. Initial permeability studies confirmed the multi-domain nature of the grains. Based on the conducted investigations and obtained results, Co^{2+} substituted Mg–Cu–Zn ferrites may be suitable for microwave absorption applications with enhanced magnetic properties.

Acknowledgements

R. C. Kambale thankfully acknowledges BCUD, Savitribai Phule Pune University for providing research funding (Grant No. RG-31).

References

[1] Shirsath SE, Kadam RH, Patange SM, *et al*. Enhanced magnetic properties of Dy^{3+} substituted Ni–Cu–Zn ferrite nanoparticles. *Appl Phys Lett* 2012, **100**: 042407.

[2] Dimri MC, Kashyap SC, Dube DC, *et al*. Complex permittivity and permeability of Co-substituted NiCuZn ferrite at rf and microwave frequencies. *J Electroceram* 2006, **16**: 331–335.

[3] Wu CP, Tung MJ, Ko WS, *et al*. Effect of neodymium substitutions on electromagnetic properties in low temperature sintered NiCuZn ferrite. *Physica B* 2015, **476**: 137–140.

[4] Rahman KR, Chowdhury F-U-Z, Khan MNI. Structural, morphological and magnetic properties of Al^{3+} substituted $Ni_{0.25}Cu_{0.20}Zn_{0.55}Al_xFe_{2-x}O_4$ ferrites synthesized by solid state reaction route. *Results in Physics* 2017, **7**: 354–360.

[5] Mohit K, Gupta VR, Rout SK. Microwave dielectric properties of $Ni_{0.2}Cu_xZn_{0.8-x}Fe_2O_4$ for application in antenna. *Prog Electromagn Res B* 2014, **57**: 157–175.

[6] Naidu KCB, Madhuri W. Microwave processed NiMg ferrite: Studies on structural and magnetic properties. *J Magn Magn Mater* 2016, **420**: 109–116.

[7] Varalaxmi N, Sivakumar KV. Structural and dielectric studies of magnesium substituted NiCuZn ferrites for microinductor applications. *Mat Sci Eng B* 2014, **184**: 88–97.

[8] Gairola SP, Verma V, Pandey V, *et al*. Modified composition of cobalt ferrite as microwave absorber in X-band frequencies. *Integrated Ferroelectrics* 2010, **119**: 151–156.

[9] Nie Y, He H, Zhao Z, *et al*. Preparation, surface modification and microwave characterization of magnetic iron fibers. *J Magn Magn Mater* 2006, **306**: 125–129.

[10] Matsumoto M, Miyata Y. Thin electromagnetic wave absorber for quasi-microwave band containing aligned thin magnetic metal particles. *IEEE T Magn* 1997, **33**: 4459– 4464.

[11] Deng L, Hagley EW, Kozuma M, *et al*. Achieving very-low-loss group velocity reduction without electromagnetically induced transparency. *Appl Phys Lett* 2002, **81**: 1168.

[12] Hwang Y. Microwave absorbing properties of NiZn–ferrite synthesized from waste iron oxide catalyst. *Mater Lett* 2006, **60**: 3277–3280.

[13] Su H, Zhang H, Tang X, *et al*. Study on low-temperature sintered NiCuZn and MgCuZn spinel ferrites. *J Alloys Compd* 2009, **475**: 683–685.

[14] Daigle A, Modest J, Geiler AL, *et al*. Structure, morphology and magnetic properties of $Mg_{(x)}Zn_{(1-x)}Fe_2O_4$ ferrites prepared by polyol and aqueous co-precipitation methods: A low-toxicity alternative to $Ni_{(x)}Zn_{(1-x)}Fe_2O_4$ ferrites. *Nanotechnology* 2011, **22**: 305708.

[15] Rezlescu E, Rezlescu N, Popa PD, *et al*. Effect of copper oxide content on intrinsic properties of MgCuZn ferrite. *Mater Res Bull* 1998, **33**: 915–925.

[16] Qi X, Zhou J, Yue Z, *et al*. Effect of Mn substitution on the magnetic properties of MgCuZn ferrites. *J Magn Magn Mater* 2002, **251**: 316–322.

[17] Xia A, Zuo C, Chen L, *et al*. Hexagonal $SrFe_{12}O_{19}$ ferrites: Hydrothermal synthesis and their sintering properties. *J Magn Magn Mater* 2013, **332**: 186–191.

[18] Yang H, Zhang X, Ao W, *et al*. Formation of $NiFe_2O_4$ nanoparticles by mechanochemical reaction. *Mater Res Bull* 2004, **39**: 833–837.

[19] Reddy MP, Madhuri W, Balakrishnaiah G, *et al*. Microwave sintering of iron deficient Ni–Cu–Zn ferrites for multilayer chip inductors. *Curr Appl Phys* 2011, **11**: 191–198.

[20] Mahmood A, Warsi MF, Ashiq MN, *et al.* Substitution of La and Fe with Dy and Mn in multiferroic $La_{1-x}Dy_xFe_{1-y}Mn_yO_3$ nanocrystallites. *J Magn Magn Mater* 2013, **327**: 64–70.

[21] Patil KC, Hegde MS, Aruna ST. *Chemistry of Nanocrystalline Oxide Materials*. World Scientific, 2008: 364.

[22] Khandekar MS, Kambale RC, Latthe SS, *et al*. Role of fuels on intrinsic and extrinsic properties of $CoFe_2O_4$ synthesized by combustion method. *Mater Lett* 2011, **65**: 2972–2974.

[23] Ghodake UR, Chaudhari ND, Kambale RC, *et al*. Effect of Mn^{2+} substitution on structural, magnetic, electric and dielectric properties of Mg–Zn ferrites. *J Magn Magn Mater* 2016, **407**: 60–68.

[24] Bhosale DN, Verenkar VMS, Rane KS, *et al*. Initial susceptibility studies on Cu–Mg–Zn ferrites. *Mater Chem Phys* 1999, **59**: 57–62.

[25] Reddy MP, Kim IG, Yoo DS, *et al*. Effect of La substitution on structural and magnetic properties of microwave treated $Mg_{0.35}Cu_{0.05}Zn_{0.60}La_xFe_{2-x}O_4$ ceramics. *Superlattice Microst* 2013, **56**: 99–106.

[26] Haque MM, Huq M, Hakim MA. Influence of CuO and sintering temperature on the microstructure and magnetic properties of Mg–Cu–Zn ferrites. *J Magn Magn Mater* 2008, **320**: 2792–2799.

[27] Sujatha Ch, Reddy KV, Babu KS, *et al*. Effects of heat treatment conditions on the structural and magnetic properties of MgCuZn nano ferrite. *Ceram Int* 2012, **38**: 5813–5820.

[28] Wagner KW. Zur Theorie der unvollkommenen Dielektrika. *Annalen der Physik* 1913, **40**: 817–855.

[29] Koops CG. On the dispersion of resistivity and dielectric constant of some semiconductors at audiofrequencies. *Phys Rev* 1951, **83**: 121.

[30] Sindhu S, Anantharaman MR, Thampi BP, *et al*. Evaluation of a.c. conductivity of rubber ferrite composites from dielectric measurements. *Bull Mater Sci* 2002, **25**: 599–607.

[31] Ahmed MA, Bishay ST. The role of Dy^{3+} ions and sintering temperature on the magnetic characterization of LiCo–ferrite. *J Magn Magn Mater* 2004, **279**: 178–183.

[32] Nikumbhn AK, Pawar RA, Nighot DV, *et al*. Structural, electrical, magnetic and dielectric properties of rare-earth substituted cobalt ferrites nanoparticles synthesized by the co-precipitation method. *J Magn Magn Mater* 2014, **355**: 201–209.

[33] Globus A. *J Phys (Paris) Colloq* 1977, **1**: C-1.

[34] Hashim M, Alimuddin, Shirsath SE, *et al*. Influence of Ni^{2+} substitution on the structural, dielectric and magnetic properties of Cu–Cd ferrite nanoparticles. *J Alloys Compd* 2013, **573**: 198–204.

[35] Nam J-H, Han W-G, Oh J-H. The effect of Mn substitution on the properties of NiCuZn ferrites. *J Appl Phys* 1997, **81**: 4794.